The Cryosphere Discuss., 7, 3823–3851, 2013
www.the-cryosphere-discuss.net/7/3823/2013/
doi:10.5194/tcd-7-3823-2013

The Cryosphere Discussions
Open Access

Albedo over snow and ice penitents

J. Abermann[1], C. Kinnard[1], and S. Lhermitte[2]

[1]Centro de Estudios Avanzados en Zonas Áridas, Raúl Bitrán s/n, Colina El Pino, La Serena, Chile
[2]Royal Netherlands Meteorological Institute (KNMI), De Bilt, the Netherlands

Received: 31 May 2013 – Accepted: 2 July 2013 – Published: 31 July 2013

Correspondence to: C. Kinnard (christophe.kinnard@ceaza.cl)

Published by Copernicus Publications on behalf of the European Geosciences Union.

Abstract

Both satellite and ground-based broadband albedo measurements over complex terrain show several limitations concerning feasibility and representativeness. In this study a series of experiments on Glaciar Tapado in the semi-arid Andes of Northern Chile is used to investigate the vertical dependence of albedo over a penitent-covered surface. The albedo–height relationship depends on the surface properties: over medium-sized snow penitents albedo increases with height, whereas over ice penitents little changes were found above the penitent tips and varying responses within the penitent troughs. The governing factor is the surface geometry and the ratio of penitent height to distance between their tips. Based on a model experiment it is shown that large parts of the variations above the tips can be explained geometrically, by varying influence of a confined albedo anomaly on a hemispherical sensor. Furthermore, the temporal evolution of broadband albedo over a penitent-covered surface is analyzed. In this context the albedo throughout two ablation seasons is discussed to place the experiments into a larger temporal context. Albedo measurements at an automated weather station show that broadband albedo over a penitents is low compared to expected values on a smooth surface. Albedo decreases early in the ablation season, and stabilizes from February onwards with variations being caused by fresh snow-fall events. The 2009/2010 and 2011/2012 seasons differ notably, where the latter shows lower albedo related to a different penitent evolution resulting in larger penitents. Finally, a comparison of the ground-based albedo observations with Landsat and MODIS-derived albedo showed that both satellite derived albedo products capture the albedo evolution with root mean square errors of 0.08 and 0.15, respectively, but also illustrate their shortcomings related to temporal resolution and spatial heterogeneity over mountain glaciers.

TCD
7, 3823–3851, 2013

1 Introduction

Surface albedo determines the short-wave radiation balance, arguably the largest energy balance component (Gardner and Sharp, 2010; Male and Granger, 1981), especially on low-latitude glaciers (e.g., MacDonell et al., 2013), where incident radiation is very high. Its spatio-temporal variations have been studied extensively using ground-based measurements (e.g., Arendt, 1999; Brock, 2004; Brock et al., 2000; Pirazzini, 2004) and various approaches show that reasonable results can be achieved using remote sensing techniques be it from satellite (Dumont et al., 2012; Klok et al., 2003; Stroeve et al., 2006) or terrestrial photography (Corripio, 2004; Dumont et al., 2011).

To ground-truth remote-sensing derived albedo with field measurements, it is important to be aware of the representativeness of the measurement site with respect to the path width of the sensor. One decisive factor for that is the "macroscopic" surface roughness of the surface, i.e. scales much larger than the wavelength of light (Wang and Zender, 2011), as studied experimentally over a sastrugi-field in Antarctica by Warren et al. (1998). At our study site, surface roughness is determined by penitents (spike formations out of snow and ice up to several meters high, Lliboutry, 1953) that form and grow as the ablation season progresses. A few studies (Corripio and Purves, 2005; Winkler et al., 2009) investigate the influence of penitents on the energy balance as a whole as they influence the aerodynamic roughness lengths and create a distinct micro-climate. Less focus has been put on how the surface roughness explicitly influences albedo and most work in this field has been done over sastrugis. Albeit being formed by entirely different physical processes, their impact and mechanisms on the optical reflectance properties are comparable. Warren et al. (1998) reviewed this issue and mention two reasons that both eventually lead to an albedo reduction. Firstly, the incident angle averaged over a field of sastrugis is lower than the solar incident angle of the respective horizontal surface if the local microtopography is taken into account. Secondly, multiple reflections between the walls occur, leading to "light-trapping" in the trough. Carroll and Fitch (1981) found that the reduction of albedo over sastrugis

TCD
7, 3823–3851, 2013

furthermore depends on the sun's position relative to the sastrugi axis. Perpendicular insolation of sastrugis reduces albedo between 2 % (Kuhn, 1974) and 4 % (Carroll and Fitch, 1981) more than parallel insolation. Pfeffer and Bretherton (1987) define the expression "effective albedo" in the context of light-trapping in crevasses as one minus the ratio of energy that is absorbed in the crevasse to the energy entering the crevasse. This concept is useful as it combines both the surface properties of the material and the light-trapping of the unevenness. They simulate numerically that, depending on the opening angle, the effective albedo can be up to 0.4 lower for a crevasse than the albedo of a flat surface. Furthermore they show that the smaller the opening angle of the crevasse (i.e. the steeper the walls), the stronger is the difference between effective albedo and the albedo of the material. Cathles et al. (2011) extended the work to differently shaped channels and crevasses and found that the effective albedo decreases with time due to changing morphologies of the roughness features. An entirely different application with similar research problems is the field of albedo evolution over urban canyons. Fortuniak (2007) presents numerical simulations of effective albedo as a function of urban canyon height-to-width ratio, showing reductions for typically occurring geometries that are in a similar order as in Pfeffer and Bretherton (1987).

Although Kotlyakov and Lebedeva (1974) noted an albedo reduction of 10 % over penitents troughs and Corripio and Purves (2005) simulated albedo decreases of 8 % compared to flat snow surfaces (Table 5 in Corripio and Purves, 2005), the effect of sensor distance on effective albedo and its spatial representativity over penitent-covered surfaces has not been studied. This effect can be crucial for satellite ground-truthing and interpretation of automated weather station (AWS) radiation data. For that reason, the aim of this paper is to analyze the vertical dependence of surface albedo over a penitent surface and its relation to geometrical surface conditions. Furthermore, we present albedo time-series for two markedly differing ablation seasons and put them in the context of satellite-derived albedo.

TCD
7, 3823–3851, 2013

2 Study site

This study was performed on Glaciar Tapado (30°08′ S 69°56′ W, Fig. 1), the largest glacier of the upper Elqui River catchment, close to the border between Chile and Argentina. The glacier is situated in the semi-arid Andes, south of the Arid Diagonal, its elevation range is between 4600 m and 5536 m (Cerro Tapado) and its size 1.05 km^2. The climate is characterized by predominantly clear skies, intense solar radiation, low air humidity and low precipitations. Higher peaks adjacent to Cerro Tapado, such as Cerro Olivares (30°17′ S 69°54′ W, 6252 m), are currently free of glaciers, suggesting that the few glaciers existing in the area are atypical features and that local climatic conditions (e.g., excess precipitation due to wind redistribution of snow) play an important role (Kull et al., 2002; Ginot et al., 2006).

3 Data and methods

3.1 Albedo vs. sensor height

To understand albedo changes with height above the surface, a tripod made out of 6 m long aluminum stakes was set up on the glacier surface over a penitent trough (Table 1, Fig. 2) at three days during the ablation season 2012/2013. A downward looking pyranometer (see Table 2 for details) was mounted to a weight hanging on a cord from the tripod top. The cord was marked every 0.5 m. During each experiment the outgoing radiation was recorded at different heights above the surface in 0.5 m-steps above the penitent tips and in 0.25 m-steps within the troughs. Simultaneously the horizontal incoming radiation was measured on a second, fixed tripod ca. 1 m above the surface in an open area where penitents were small enough to avoid reducing the field of view of the upward-looking sensor. The distance between the second tripod and the downward-looking sensor was set large enough to avoid mutual influence. All experiments were performed under cloud-free conditions with no or negligible wind to avoid

TCD
7, 3823–3851, 2013

movement of the downward looking pyranometer. Based on the incoming and outgoing radiation albedo was calculated for each experiment (α) and the vertical albedo dependence was defined as $\varepsilon = \frac{d\alpha}{dz}$. Figure 3 shows a schematic view of the experiment and the abbreviations and symbols used therein.

3.2 Temporal albedo evolution

To analyze the evolution of broadband albedo over a penitent-covered surface. an automated weather station (AWS) was operated in the ablation zone of Glaciar Tapado (Fig. 1) during two ablation seasons (2009–2010; 2011–2012). Short-wave radiation was measured every 10 s and averaged to hourly values. Sensor specifications are summarized in Table 2. The radiation sensor was installed horizontally over a 10° inclined surface with an aspect of 134° (values derived from a 2010 GeoEye DEM, resampled to 20 m cell-size). The same correction as in Abermann et al. (2013) following Grenfell et al. (1994) has been applied to adjust albedo for the slightly sloping surface, however deviations from the uncorrected data are minimal as radiation values are close to solar noon and the aspect of the surface is not very different from the North–South axis.

The AWS albedo measurements subsequently were compared to satellite-derived albedo from MODIS and Landsat sensors. In this context MODIS albedo (α_{MOD}) was derived from the MODIS daily snow product (MOD10A1) processed by the National Snow and Ice Data Center (Stroeve et al., 2006; Hall et al., 2007). MOD10A1 provides daily estimates of the snow cover, snow fraction and albedo of snow surfaces at 500 m spatial resolution based on the Terra overpass (i.e., around 10:30 LST at the equator) with viewing angle closest to nadir. Additionally, Landsat albedo (α_{L7}) was derived over a square of nine pixels surrounding the AWS location from Landsat ETM+ images. 13 Landsat ETM+ images above the Tapado region were selected over both ablation seasons based on data availability of cloud-free Landsat scenes (both visually and from metadata). Landsat ETM+ data provides spectral radiance in seven bands at the top of the atmosphere (30 m spatial resolution, 16 day temporal resolution, acquisition around

TCD
7, 3823–3851, 2013

10:00 LST at the equator), which was converted to Landsat spectral reflectance at the surface and broadband albedo using the methodology of Klok et al. (2003) based on the anisotropic reflection factor of snow/ice in combination with the parameterization of Knap et al. (1999).

4 Results

4.1 Albedo vs. sensor height

Figure 4 shows the albedo changes with sensor height above the surface. Details on time and geometry are given in Table 1. During experiment A, when snow penitents were ∼ 1 m high and the tips of the individual penitents closely spaced (H/D: 0.5), albedo rose from 0.25 at 0.5 m to 0.35 at 4 m above the ground. ε is highest in the lowest meter (i.e. between the trough and tip of penitents) but stays positive higher up. Experiment B shows a higher H/D-ratio (1.2) and a less distinct elevation-dependence: between 0.5 m and 4 m albedo reduces by 3–4 %. The two last experiments (C and D) have been carried out on the same day (19 April 2013) at nearby locations (ca. 15 m apart), but with differences in surface geometry. Experiment C was performed over small penitents which were rather far apart (H/D: 2.1), whereas D was made over a deep and narrow trough (H/D: 0.7). Both experiment B and C, on one hand, and A and D, on the other hand, show similar albedo changes with sensor height above the surface. B and C show an albedo reduction of ca. 3 % between 0.5 and 1 m, whereas A and D show a pronounced positive ε in the lowest 1.5 m leading to an albedo-increase of ca. 0.1. At 1.5 m above the surface the C and D curves converge with differences of less than 2 %. An albedo increase is notable up to 3 m over the small snow penitents (A), whereas it stabilizes over large ice penitents after 1.5 m (D).

TCD
7, 3823–3851, 2013

4.2 Temporal albedo evolution

Figure 5 shows the temporal evolution of both satellite and ground based broadband albedo for the 2009/2010 and 2011/2012 seasons. Both seasons differ significantly in their albedo evolution. 2009/2010 started with higher albedo values of more than 0.6 and then continuously reduced until mid-January, where a significant snowfall event raised albedo to 0.8 after which metamorphosis and ice-exposure reduced it again to 0.2. In 2011/2012, values in early December were around 0.45. Throughout the season several fresh snow events temporarily raised albedo. From late January onwards the ie albedo showed values of about 0.25–0.30.

Comparison of the ground-based albedo observations with Landsat and MODIS derived albedo show that both satellite derived albedo products capture the albedo evolution including snowfall events (mean difference of −0.019 and root mean square difference of 0.08 (Landsat: 13 images) and mean difference of −0.119 and root mean square difference of 0.15 (MODIS: 35 images), respectively), but also illustrate their shortcomings with clear biases (e.g., MODIS albedo underestimation in 2009/2010 with deviations of up to 0.22) that complicate the monitoring of albedo evolutions among seasons.

5 Discussion

Various processes determine the albedo changes with sensor height above the surface, where the influence of an albedo anomaly on the recorded signal of a hemispherical sensor plays a key role. To illustrate this assume a surface with a constant albedo and a local negative albedo anomaly, such as a patch of dirty ice. A hemispherical pyranometer placed over the albedo anomaly and moved upward will record a positive ε as the sensor progressively integrates a larger fraction of the surrounding surface and less of the local feature below. The trend is reversed, i.e. negative ε, if the local albedo anomaly below the sensor is positive (larger than the surrounding surface). When the

TCD
7, 3823–3851, 2013

sensor is high enough, the field of view of the local albedo anomaly below becomes infinitely small and the measured albedo approximates the albedo of the surrounding surface (ε close to 0). This process happens within the trough, when, for instance the trough's bottom has a lower material albedo than the penitent walls due to either dust, debris or to melt. Further away from the bottom, the influence of this negative anomaly decreases, and the recorded albedo increases (e.g. experiment A).

Shading and multiple reflections also have an important effect on albedo changes with sensor height within the trough since they alter the direct and diffuse radiation, respectively. The amount of shading within the penitent trough depends on the sun's zenith angle and the penitent geometry. In Fig. 6 we computed the maximum penetration depth of direct sunlight H_{max} (see Fig. 3) in a penitent trough of triangular shape and varying tip-distances D (according to the values from the experiments) as a function of varying solar zenith angles ξ. Direct radiation can penetrate deeper in the penitent trough with larger D and smaller ξ. When H is smaller than H_{max} for a given D, it implies the entire trough is directly sunlit. The points in Fig. 6 show ξ vs. H for each experiment. It is evident, that for A, B and C the trough's bottom are directly sunlit whereas in D the lowest meter was shaded. As the effective albedo is calculated by scaling the measured outgoing radiation in the trough with the incoming radiation that is not influenced by the penitents, part of α_{eff} reduction in the lowest meter of experiment D can be explained from reduced incoming radiation due to shading within the trough. These strong albedo reductions due to shading are not apparent in A–C as here the shading effects are much smaller.

The local diffuse radiation within the trough is composed of atmospheric diffuse solar radiation and the multiple reflections from the penitent walls. Diffuse solar radiation increases with an increasing sky view factor and thus with distance from the bottom, whereas multiple reflections decrease with height for an entirely lit trough (Corripio and Purves, 2005). Multiple reflections in the trough are a function of the penitent geometry (ratio H/D, see Fig. 3), and are more efficient for small H/D (i.e. small and/or narrow penitents). Assuming a constant material albedo, this effect would lead to a negative

TCD
7, 3823–3851, 2013

ε within the trough. However, as, depending on the zenith angle, it is more likely that part of trough is shaded, the shading effects predominates and results in a positive ε. These explanations contrast with experiment A, which shows a small H/D and a pronounced increase in albedo from the trough bottom up to the penitent tip, although direct radiation hits the trough's bottom (Fig. 6). Nevertheless, Fig. 2 shows that parts of the penitent walls were shaded during experiment A. Hence it is likely that shading dominates the upward trend in albedo within the trough. Experiment B and C show a slight albedo increase downward from the trough's tip, because the entire trough is illuminated directly, which indicates a stronger influence of the multiply reflected direct radiation from the penitent walls. The trend reverses near the trough bottom, which in the case of experiment B was due to the sensor being close to running water, and over refrozen ice at the bottom of D. Generally we found that too many unknowns exist to model the albedo evolution within the trough in a simple manner, and that more detailed measurements of penitent morphology combined with sophisticated numerical models are crucial to disentangle the various processes.

The albedo variations above the penitent tips can be mainly explained by the aforementioned effect of an albedo anomaly measured by a hemispherical sensor and are caused by randomly varying changes in facies, dust concentration, superficial melt water and roughness. The surface of a penitent covered glacier appears homogeneous when seen from a distance, while in reality, random variations in penitent morphology occur. The effective albedo (α_p) of a penitent trough, as measured from the level of the tip in each experiment, represents one sample from a distribution with unknown population mean μ_{α_p} and variance $\mu^2_{\alpha_p}$. μ_{α_p} corresponds to the average penitent trough albedo over the whole surface. Moving the hemispherical pyranometer upward above a penitent trough will then result in a trend in effective albedo whose sign and magnitude will depend on how large the difference is between the penitent trough albedo below the sensor and the population mean μ_{α_p}. Considering an infinite rough surface which reflects isotropically (i.e. without directional dependence of the reflected radiation), the variation of albedo with height above a penitent trough as measured by a

TCD
7, 3823–3851, 2013

hemispherical sensor can be modeled as:

$$\alpha_{\text{eff}}(z) = \alpha_{\text{p}} \int_{\theta=0}^{\theta=i} \cos\theta \mathrm{d}\theta + \bar{\alpha}_{\text{p}} \int_{\theta=i}^{\theta=\pi/2} \cos\theta \mathrm{d}\theta \quad (1)$$

Where $\alpha_{\text{eff}}(z)$ is the measured effective albedo above a penitent trough at height z_{p} above the tip (see Fig. 3), θ is the sensor viewing angle measured positively from nadir, $i = \text{atan}(2D/z)$ is the maximum viewing angle of the penitent trough with diameter D, α_{p} is the effective albedo of the penitent trough (measured at the level of the tip) and $\bar{\alpha}_{\text{p}}$ is the sample average of penitent trough effective albedo over the whole surface. Assuming that the penitent morphology is stationary in space (no trend over the surrounding surface), then, as the sensor moves up, it averages an increasing number of penitents from the surrounding surface and eventually tends toward the population mean, as:

$$z_{\text{p}} \Rightarrow \infty, \text{ then } \alpha_{\text{eff}} \Rightarrow \bar{\alpha}_{\text{p}} \Rightarrow \mu_{\alpha_{\text{p}}} \quad (2)$$

In Eq. (1) a constant value has to be assumed for $\bar{\alpha}_{\text{p}}$ which is then considered to be the best estimator of $\mu_{\alpha_{\text{p}}}$. In reality, $\bar{\alpha}_{\text{p}}$ varies randomly but progressively converges to $\mu_{\alpha_{\text{p}}}$ as the height increases, due the law of large numbers (Hsu and Robbins, 1947). Integrating Eq. (1) gives:

$$\alpha_{\text{eff}}(z) = \alpha_{\text{p}} \sin(i) + \bar{\alpha}_{\text{p}}[1 - \sin(i)] \quad (3)$$

A first estimate of $\bar{\alpha}_{\text{p}}$ can be obtained by using the highest measured value (Fig. 4). The trend between the top of penitents and the highest measured value is in general well reproduced by Eq. (3) (Fig. 7, red lines). However since we do not know if the sensor was high enough to truly approximate $\bar{\alpha}_{\text{p}}$, another approach is to fit Eq. (3) to the data (Fig. 7, green lines) which allows deriving a theoretical estimate for $\bar{\alpha}_{\text{p}} = \mu_{\alpha_{\text{p}}}$,

TCD
7, 3823–3851, 2013

for an infinite height ($z = \infty$). Equation (3) was fitted to measured $\alpha_{\text{eff}}(z)$ and α_{p} using a Trust-Region-Reflective least squares algorithm. We can define a limiting height at which the measured albedo reaches 1 % of the theoretical mean albedo:

$$\alpha_{\text{eff}}(z) - \bar{\alpha}_{\text{p}} = \sin(i)\left(\alpha_{\text{p}} - \bar{\alpha}_{\text{p}}\right) = \pm 0.01\bar{\alpha}_{\text{p}} \quad (4)$$

Equation (4) can be solved for i and then for $z = 2D/\tan(i)$, giving an effective height at which the measured albedo is within 1 % of the theoretical population average (Table 3).

The results show that the difference between α_{p} and $\bar{\alpha}_{\text{p}}$ is overall small, being largest for experiment A (6 %) while it is 2 % for B and D and < 1 % for C. Modeling results show that the sensor needs to be between 2 m and 8 m above the penitent's tip to be within 1 % of the theoretical average (Table 3). In practice however, the effective albedo of penitents' troughs as measured at the tip level is within the 95 % confidence interval around the theoretical mean for experiments B, C and D, and only experiment A shows a significant deviation of 0.06. Placing the sensor at a height equal to twice the penitent height ($2H$) further reduces the difference to less than ±0.01. These results show that the albedo time series presented in Fig. 5 are representative for the surface surrounding the AWS and not only of the albedo anomaly within the penitent trough below the sensor, as the sensor was fixed initially 1–1.7 m above the snow surface before significant development of penitents began. They further support the use of these time series for calibrating or validating albedo retrieval algorithm from satellites (Box et al., 2012; Dumont et al., 2012) or terrestrial photographs (Corripio, 2004; Dumont et al., 2011).

The comparison of experiment C and D is useful to show an example for the random distribution of ice penitents and the resulting variations in vertical albedo evolution as they are both performed on the same day at very nearby locations. The convergence of the two curves above 1.5 m confirms the explanation given above that the penitent field's mean is closely represented above the penitent tips albeit the very different individual morphologies. The difference in albedo time series between the seasons is clearly attributable to a very distinct evolution of penitents (Fig. 8). Whereas in 2009/2010 penitents started to form in December and did not get higher than one meter

TCD
7, 3823–3851, 2013

before February, in 2011/2012 there were already small penitents during the first visit in late November and by February they were higher than 1.5 m. This confirms what previous studies (Corripio and Purves, 2005; Kotlyakov and Lebedeva, 1974; Pfeffer and Bretherton, 1987) indicate: generally penitents decrease surface albedo compared to flat surfaces.

The seasonal development is also clearly visible in the Landsat- and MODIS-derived albedos, where in this study a similar correspondence (mean difference of 0.119) between AWS and MODIS-derived albedo over mountain glaciers are obtained then in Dumont et al. (2012) (mean difference of 0.11). On the other hand, lower correspondence than Box et al. (2012) is obtained, but they focused on monthly averages over more homogenous surfaces on the Greenland ice sheet. The Landsat albedo shows a better correspondence (mean underestimation of −0.019) with the AWS albedo than the MODIS-derived albedo. These accuracies are in the order of magnitude of the Landsat albedo accuracies derived by Klok et al. (2003), who found an overestimation of 0.03, but with lower root mean square difference (0.07). Possible explanations for the biases between Landsat-derived and AWS albedo are the spatial heterogeneity (i.e., the experiment footprint is smaller than 9×30 m) in dust and debris cover, in combination with the assumption of a flat surface in the anisotropic reflection factor, which is certainly not the case for penitents fields. This can also be seen in Table 3, where the effective albedo of the experiments is compared with the Landsat-derived albedo of the closest date (i.e., under different illumination conditions due to different date/hour results in changes in the solar zenith angle of $\sim 10^{\circ}$) and where different biases occur when the penitents further develop.

The higher accuracy for the Landsat albedo compared to the MODIS albedo likely is related to the improved spatial resolution of the Landsat pixels (30 m vs. 500 m). In this context and given the spatial extent of the glacier, the MODIS-derived albedo is probably more related to the combination of glacier and surrounding surface albedo. This spatial heterogeneity also explains the lower than daily temporal resolution of the MODIS albedo, although daily albedo values should be retrieved given the daily

TCD
7, 3823–3851, 2013

MODIS overpass. In reality, however, this daily temporal resolution is not obtained for the MOD10A1 product as the glacier is often misclassified as land/cloud. These misclassifications (i.e., only 15 % of the observations is classified as snow/ice, vs. 78 % land and 7 % cloud) show that the commonly reported snow vs. cloud misclassification (e.g., Dozier et al., 2008) does not play an important role in this area with low cloud cover (Gascoin et al., 2013), but that glacier's snow/ice cover is often not detected in the MOD10A1 product as it only covers a subpixel fraction with snow/ice. This misclassification effect due to surrounding land will moreover be enhanced as the pixel footprint of the MODIS sensor is often much larger than 500 m due to off-nadir viewing conditions (Dozier et al., 2008). As such, the advantage of the MOD10A1 product (i.e., daily temporal resolution) is relatively small compared to the spatial resolution of Landsat to retrieve effective albedo over small mountain glaciers with large spatial variability.

6 Conclusions

It has been shown that albedo varies within the troughs and above the tips of snow and ice penitents. Measuring albedo anomalies of a rough surface using a downward looking pyranometer with a hemispherical view is the main cause for these height variations above the tip. We show that albedo measurements above the tip do not differ significantly from the surrounding surface average, supporting the use of AWS-equipped pyranometers located above the penitent tips to monitor albedo over penitents-covered glaciers and to calibrate or validate remotely-sensed albedo. Within the trough of the penitents a complex combination of factors occurs and additional work is required to model them adequately. Numerical simulations on a small scale analogue to Cathles et al. (2011) or Fortuniak (2007) and/or laboratory experiments similar to Bergeron et al. (2006) but more specifically addressing the problems raised in the present study may help to increase this understanding. As a model input more detailed high-resolution measurements are necessary and we strongly encourage repeating analogue experiments more frequently in another early season. The comparison of the

TCD
7, 3823–3851, 2013

ground-based effective albedo observations with Landsat and MODIS-derived albedo showed that both satellite derived albedo products capture the albedo evolution, but also illustrate the problems related to temporal resolution and spatial heterogeneity over heterogeneous glaciers.

Acknowledgements. The authors would like to acknowledge the financial support of Fondo Nacional de Desarollo Científico y Tecnológico (Fondecyt project No. 1130598), the Dirección General de Agua Chile (DGA) and the Centro del Agua para Zonas Aridas y Semiáridas de América Latina y El Caribe (CAZALAC) for ongoing studies at Glaciar Tapado. S. Lhermitte was supported in the framework of project GO-OA-25 funded by Netherlands Organisation for Scientific Research (NWO) and as postdoctoral researcher for Fonds Wetenschappelijk Onderzoek – Vlaanderen. Thanks D. Uribe Jofré for support during the experiments, the CEAZA glaciology group for maintaining the AWS and M. Kuhn for his comments.

References

Abermann, J., Kinnard, C., and MacDonell, S.: Albedo variations and the impact of clouds on glaciers in the Chilean semi-arid Andes, J. Glaciol., submitted, 2013.

Arendt, A.: Approaches to modelling the surface albedo of a high arctic glacier, Geogr. Ann. A, 81, 477–487, doi:10.1111/1468-0459.00077, 1999.

Bergeron, V., Berger, C., and Betterton, M. D.: Controlled irradiative formation of penitentes, Phys. Rev. Lett., 96, 098502, doi:10.1103/PhysRevLett.96.098502, 2006.

Box, J. E., Fettweis, X., Stroeve, J. C., Tedesco, M., Hall, D. K., and Steffen, K.: Greenland ice sheet albedo feedback: thermodynamics and atmospheric drivers, The Cryosphere, 6, 821–839, doi:10.5194/tc-6-821-2012, 2012.

Brock, B. W.: An analysis of short-term albedo variatons at Haut Glacier d'Arolla, Switzerland, Geogr. Ann. A, 86, 53–65, doi:10.1111/j.0435-3676.2004.00213.x, 2004.

Brock, B. W., Willis, I. C., and Sharp, M. J.: Measurement and parameterization of albedo variations at Haut Glacier d'Arolla, Switzerland, J. Glaciol., 46, 675–688, 2000.

Carroll, J. J. and Fitch, B. W.: Effects of solar elevation and cloudiness on snow albedo at the South Pole, J. Geophys. Res., 86, 5271, doi:10.1029/JC086iC06p05271, 1981.

TCD
7, 3823–3851, 2013

Cathles, L. M., Abbot, D. S., Bassis, J. N., and MacAyeal, D. R.: Modeling surface-roughness/solar-ablation feedback: application to small-scale surface channels and crevasses of the Greenland ice sheet, Ann. Glaciol., 52, 99–108, doi:10.3189/172756411799096268, 2011.

Corripio, J. G.: Snow surface albedo estimation using terrestrial photography, Int. J. Remote Sens., 25, 5705–5729, doi:10.1080/01431160410001709002, 2004.

Corripio, J. G. and Purves, R. S.: Surface energy balance of high altitude glaciers in the Central Andes: the effect of snow penitentes, in: Climate and Hydrology of Mountain Areas, edited by: de Jong, C., Collins, D. N., and Ranzi, R., John Wiley & Sons, Ltd., New York, 15–28, 2005.

Dozier, J., Painter, T. H., Rittger, K., and Frew, J. E.: Time-space continuity of daily maps of fractional snow cover and albedo from MODIS, Adv. Water Resour., 31, 1515–1526, doi:10.1016/j.advwatres.2008.08.011, 2008.

Dumont, M., Sirguey, P., Arnaud, Y., and Six, D.: Monitoring spatial and temporal variations of surface albedo on Saint Sorlin Glacier (French Alps) using terrestrial photography, The Cryosphere, 5, 759–771, doi:10.5194/tc-5-759-2011, 2011.

Dumont, M., Gardelle, J., Sirguey, P., Guillot, A., Six, D., Rabatel, A., and Arnaud, Y.: Linking glacier annual mass balance and glacier albedo retrieved from MODIS data, The Cryosphere, 6, 1527–1539, doi:10.5194/tc-6-1527-2012, 2012.

Fortuniak, K.: Numerical estimation of the effective albedo of an urban canyon, Theor. Appl. Climatol., 91, 245–258, doi:10.1007/s00704-007-0312-6, 2007.

Gardner, A. S. and Sharp, M. J.: A review of snow and ice albedo and the development of a new physically based broadband albedo parameterization, J. Geophys. Res., 115, F01009, doi:10.1029/2009JF001444, 2010.

Gascoin, S., Lhermitte, S., Kinnard, C., Bortels, K., and Liston, G. E.: Wind effects on snow cover in Pascua-Lama, Dry Andes of Chile, Adv. Water Resour., 55, 25–39, doi:10.1016/j.advwatres.2012.11.013, 2013.

Ginot, P., Kull, C., Schotterer, U., Schwikowski, M., and Gäggeler, H. W.: Glacier mass balance reconstruction by sublimation induced enrichment of chemical species on Cerro Tapado (Chilean Andes), Clim. Past, 2, 21–30, doi:10.5194/cp-2-21-2006, 2006.

Grenfell, T., Warren, S. G., and Mullen, P.: Reflection of solar radiation by the Antarctic snow surface at ultraviolet, visible, and near-infrared wavelengths, J. Geophys. Res., 99, 18669–18684, doi:10.1029/94JD01484, 1994.

TCD
7, 3823–3851, 2013

Hall, D. K., Riggs, G. A., and Salomonson, V. V.: MODIS/Aqua Snow Cover Daily L3 Global 500 m Grid V005, version 5, 2008, 2009, National Snow and Ice Data Center, Boulder, Colorado, USA, Digital media, 2007 (updated daily).
Hsu, P. L. and Robbins, H.: Complete convergence and the law of large numbers, P. Natl. Acad. Sci. USA, 33, 25–31, doi:10.1007/978-1-4684-9324-5_29, 1947.
Klok, E., Greuell, W., and Oerlemans, J.: Temporal and spatial variation of the surface albedo of Morteratschgletscher, Switzerland, as derived from 12 Landsat images, J. Glaciol., 49, 491–502, 2003.
Knap, W. H., Reijmer, C. H., and Oerlemans, J.: Narrowband to broadband conversion of Landsat TM glacier albedos, Int. J. Remote Sens., 20, 2091–2110, 1999.
Kotlyakov, V. M. and Lebedeva, I. M.: Nieve and ice penitentes. Their way of formaton and indicative significance, Zeitschrift für Gletscherkunde und Glazialgeologie, 10, 111–127, 1974.
Kuhn, M.: Anisotropie reflection from sastrugi flelds, Antarct. J. US, 9, 123–124, 1974.
Kull, C., Grosjean, M., and Veit, H.: Modeling modern and late pleistocene glacio-climatological conditions in the North Chilean Andes (29–30°), Climate Change, 52, 359–381, 2002.
Lliboutry, L.: The origin of penitents, J. Glaciol., 2, 331–338, 1953.
MacDonell, S., Kinnard, C., Mölg, T., Nicholson, L., and Abermann, J.: Meteorological drivers of ablation processes on a cold glacier in the semiarid Andes of Chile, The Cryosphere Discuss., 7, 1833–1870, doi:10.5194/tcd-7-1833-2013, 2013.
Male, D. H. and Granger, R. J.: Snow surface energy exchange, Water Resour. Res., 17, 609–627, doi:10.1029/WR017i003p00609, 1981.
Pfeffer, W. T. and Bretherton, C. S.: The effect of crevasses on the solar heating of a glacier surface, IAHS Red Book, 170, 191–206, 1987.
Pirazzini, R.: Surface albedo measurements over Antarctic sites in summer, J. Geophys. Res., 109, D20118, doi:10.1029/2004JD004617, 2004.
Stroeve, J. C., Box, J. E., and Haran, T.: Evaluation of the MODIS (MOD10A1) daily snow albedo product over the Greenland ice sheet, Remote Sens. Environ., 105, 155–171, doi:10.1016/j.rse.2006.06.009, 2006.
Wang, X. and Zender, C. S:. Arctic and Antarctic diurnal and seasonal variations of snow albedo from multiyear Baseline Surface Radiation Network measurements. J. Geophys. Res., 116, F03008, doi:10.1029/2010JF001864, 2011.

TCD
7, 3823–3851, 2013

Warren, S. G., Brandt, R. E., and O'Rawe Hinton, P.: Effect of surface roughness on bidirectional reflectance of Antarctic snow, J. Geophys. Res., 103, 25789–25807, doi:10.1029/98JE01898, 1998.

Winkler, M., Juen, I., Mölg, T., Wagnon, P., Gómez, J., and Kaser, G.: Measured and modelled sublimation on the tropical Glaciar Artesonraju, Perú, The Cryosphere, 3, 21–30, doi:10.5194/tc-3-21-2009, 2009.

TCD
7, 3823–3851, 2013

Table 1. Details of the individual experiments. ξ is the solar zenith angle and Φ the sun's azimuth angle during the experiment, H is the penitent height (tip to trough) of the closest penitent, D the distance between the nearest penitents' tips. The ratio H/D is dimensionless.

	Date	Hour [SLT]	ξ [°]	Φ[°]	H [m]	D [m]	D/H [ ]	Surface type
A	07 Dec 2012	13:30	15	296	1.0	0.5	0.5	Snow
B	21 Mar 2013	13:00	31	353	2.1	2.5	1.2	Ice
C	19 Apr 2013	12:30	42	3	0.9	1.9	2.1	Ice
D	19 Apr 2013	13:40	44	338	2.0	1.4	0.7	Ice

TCD
7, 3823–3851, 2013

Table 2. Sensor specifications and accuracies. The same type of sensors has been deployed on both AWS. The instrument heights give minimum and maximum values.

	Device	Accuracy	Spectral range	instrument height
Radiation at AWS	Kipp and Zonen CNR1	±10 % on daily totals	305 to 2800 nm	2009/2010: 1.72–4.02 m 2011/2012: 1.00–3.75 m
Experiment A–D	Apogee SP212 and SP215	±5 %	320 to 1120 nm	0.25–4.5 m

TCD
7, 3823–3851, 2013

Table 3. Geometrical conditions (H and D), the measured effective albedo at H (α_p) and $2H$ (α_{eff} $2H$), the theoretical mean penitent field's albedo $\bar{\alpha}_p$, the limiting effective height z ($0.99\bar{\alpha}_p$), the difference between $\bar{\alpha}_p$ and α_p, the difference between $\bar{\alpha}_p$ and α_{eff} at $z = 2H$, the Landsat albedo α_{L7} with acquisition date, and the MODIS albedo α_{MO} with acquisition date for the four experiments. MODIS and Landsat acquisition times are around 10:30 and 10:00 LST at the equator, respectively.

Experiment	H (m)	D (m)	α_p	$\bar{\alpha}_p$	$\bar{\alpha}_p$ 95%	z (0.99 $\bar{\alpha}_p$) (m)	$\bar{\alpha}_p - \alpha_p$	α_{eff} $2H$	$\bar{\alpha}_p - \alpha_{eff}$ $2H$	α_{L7}	α_{MOD}
A	1.0	0.5	0.32	0.39	±0.01	4.1	0.06	0.38	0.01	0.39 (13 Dec)	–
B	2.1	2.5	0.28	0.30	±0.02	8.3	0.02	0.30	0.004	0.24 (19 Mar)	0.17 (23 Mar)
C	0.9	1.9	0.33	0.32	±0.01	2.1	−0.01	0.33	−0.01	0.24 (20 Apr)	0.35 (29 Apr)
D	2.0	1.4	0.34	0.32	±0.02	4.4	−0.02	0.32	−0.01	0.24 (20 Apr)	0.35 (29 Apr)

TCD
7, 3823–3851, 2013

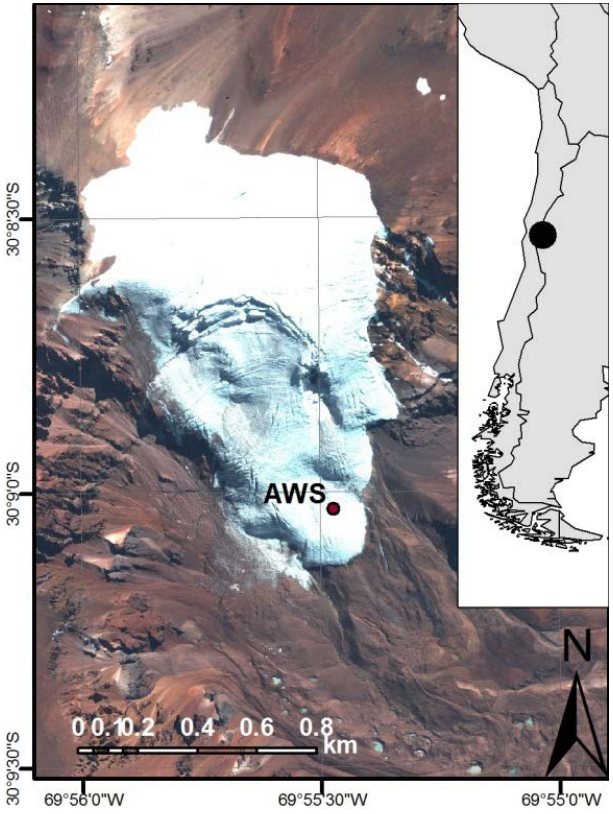

Fig. 1. Glaciar Tapado with the location of the AWS where albedo experiments were carried out. The inset shows the location in South America close to the Chilean–Argentinean border.

TCD
7, 3823–3851, 2013

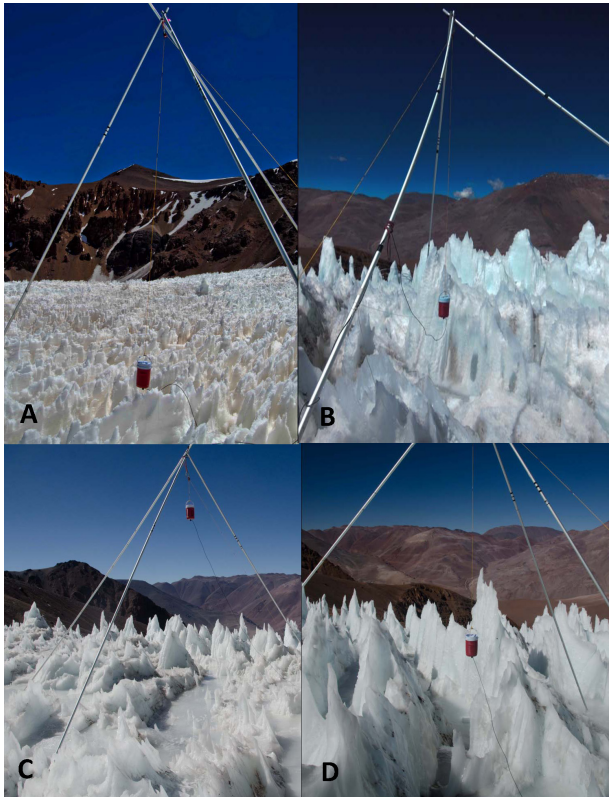

Fig. 2. The four experiments capturing different surfaces. Details for the experiments A–D are listed in Table 1.

TCD
7, 3823–3851, 2013

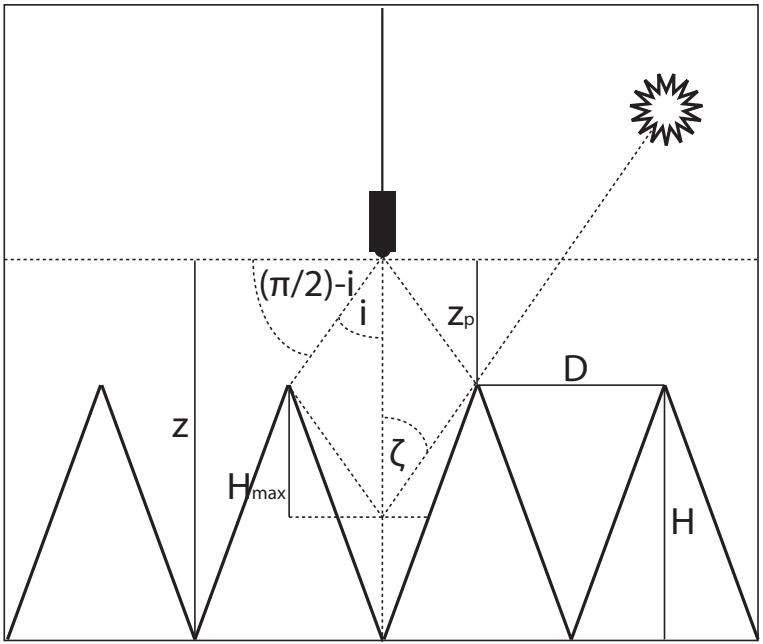

Fig. 3. A conceptual view of triangular-shaped penitents and the angles and geometrical features described in the text.

TCD
7, 3823–3851, 2013

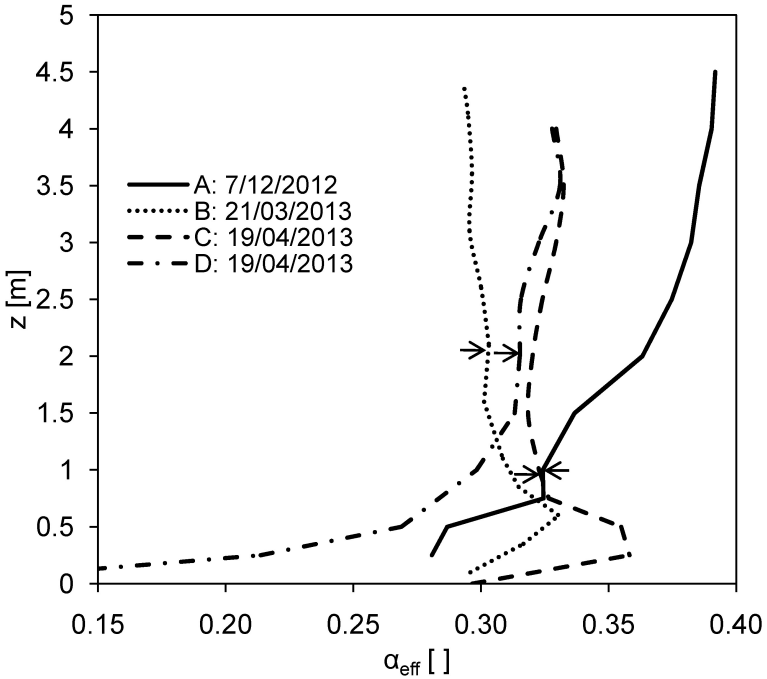

Fig. 4. Effective broadband albedo vs. height above surface for the four experiments. The arrows point to the tip of the penitents at the respective experiment.

TCD
7, 3823–3851, 2013

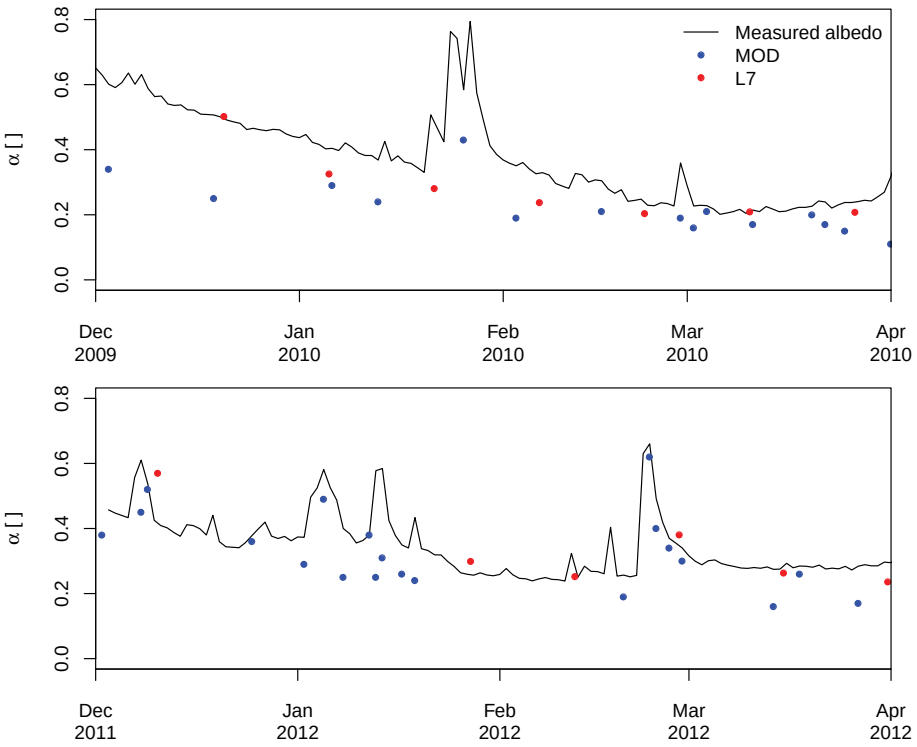

Fig. 5. Seasonal evolution of broadband albedo on Glaciar Tapado for the ablation seasons 2009/2010 **(a)** and 2011/2012 **(b)**. The solid lines are arithmetic means of hourly values (slope corrected) between 10 and 11 Local Solar Time (LST) for every day at the AWS, whereas the dots represent the MODIS (MOD: Terra overpass at 10:30 LST at the equator) and Landsat (overpass at 10:00 LST at the equator) derived albedos.

TCD
7, 3823–3851, 2013

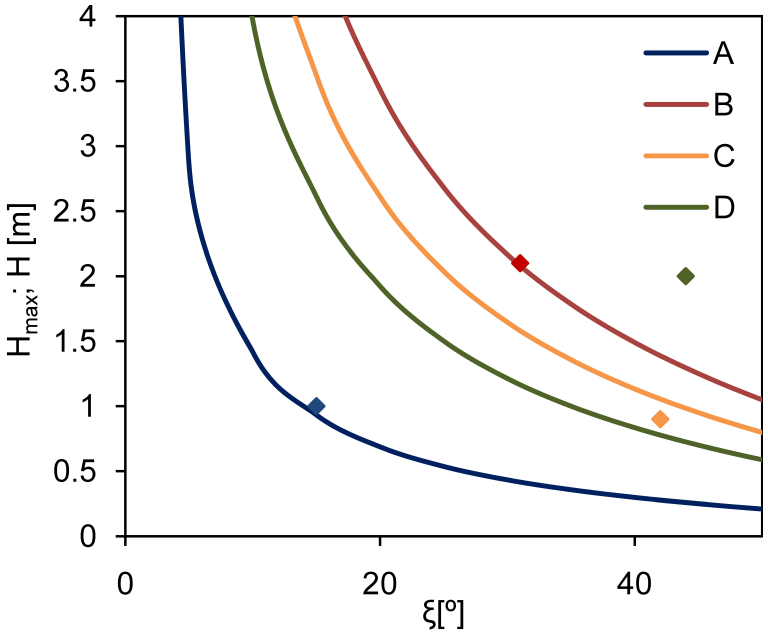

Fig. 6. Solar zenith angle ξ vs. the maximum penetration depth of direct radiation H_{max} (lines) for the distances of penitent-tips of the experiments A–D, assuming a triangular-shaped penitent-field with the sun standing perpendicular to the rows. The points indicate ξ vs. H as they occurred during the experiment.

TCD
7, 3823–3851, 2013

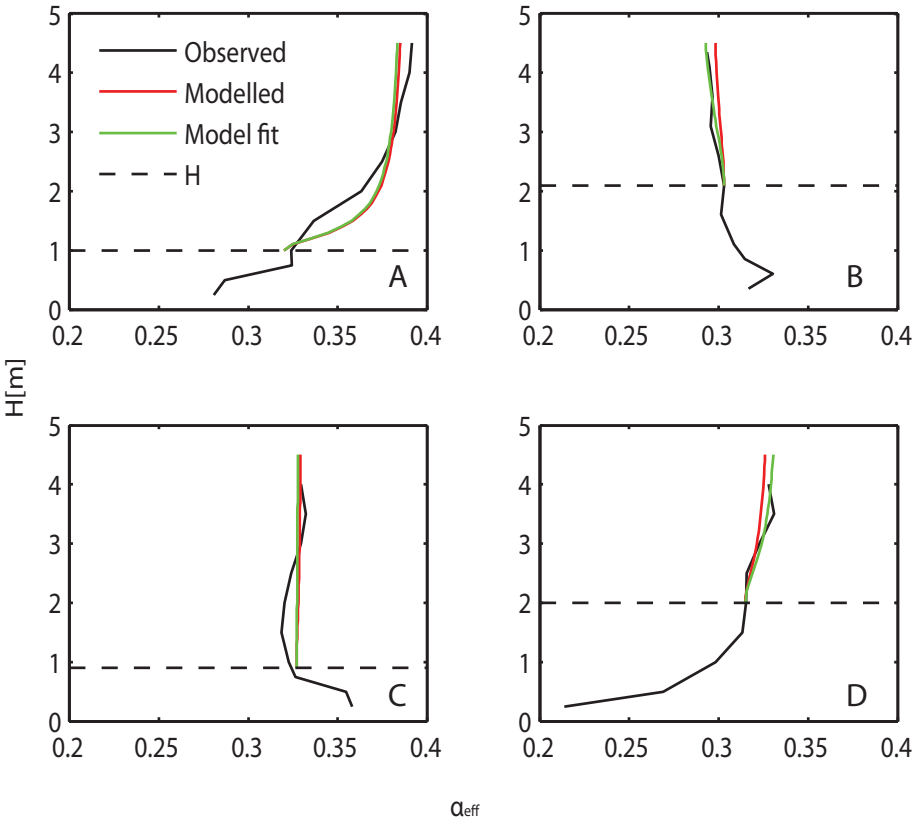

Fig. 7. Effective albedo vs. height: measured (black), modelled (red) and modelled with fitting as explained in the text (green). The dashed line displays *H* for each experiment.

TCD
7, 3823–3851, 2013

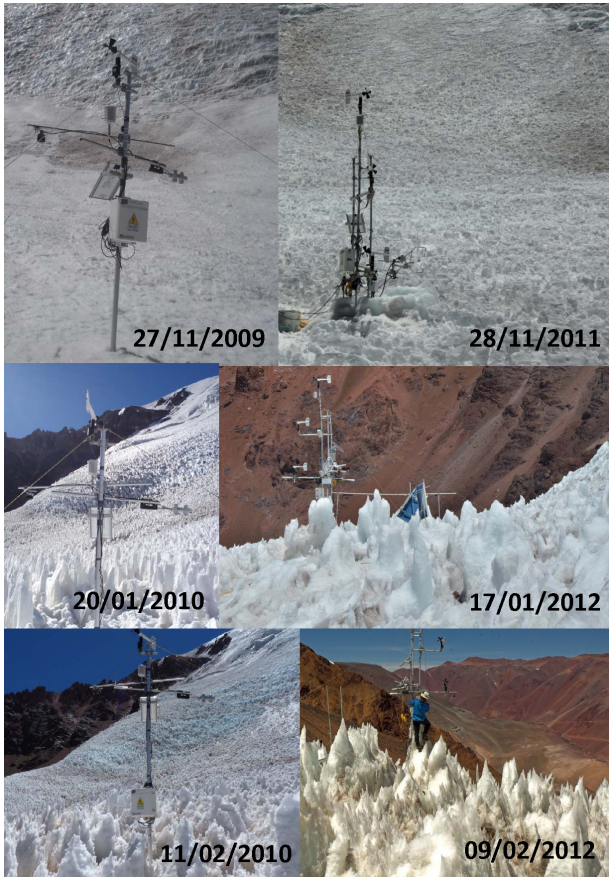

Fig. 8. Compilation of photographs from the AWS during the seasons 2009/2010 (left side) and the respective nearest available point in time of 2011/2012 (right side). Note the different penitent height from the beginning and their evolution throughout the season (Fotos: CEAZA glaciology group).

TCD
7, 3823–3851, 2013